# 6

# PLASMON ABSORPTION OF EMBEDDED NANOPARTICLES

A. Heilmann

*Fraunhofer Institute for Mechanics of Materials, Halle (Saale), Germany*

## 1. INTRODUCTION

The optical properties of metal nanoparticles embedded in an insulating host differ substantially from the optical properties of bulk metals. Under the influence of an electrical field, there is a plasmon excitation of the electrons at the particle surface. This resonance, which takes place at a certain energy of the incident light, results in an optical absorption, the so-called plasmon absorption or plasma resonance absorption [1, 2].

The excitation of the surface plasmon is found to be an extinction maximum or transmission minimum. The spectral position $\tilde{\nu}_r$, half-width (full width at half-maximum) $\Gamma$ and relative intensity $I_r$ depend on various physical parameters. First, the dielectric functions of the metal $\hat{\varepsilon}_{me}(\tilde{\nu})$ and of the polymer $\hat{\varepsilon}_{po}(\tilde{\nu})$ are involved. Second, the particle size and shape distribution play an important role. Third, the interfaces between particles and the surrounding medium, the particle–particle interactions, and the distribution of the particles inside the insulating material have to be considered. For a description of the optical plasmon resonance of an insulating material with embedded particles, a detailed knowledge of the material constants of insulating host and of the nanoparticles

*Metal-Polymer Nanocomposites*, Edited by Luigi Nicolais and Gianfranco Carotenuto
ISBN 0-471-47131-3 

as well as of the nanostructural properties is necessary. In addition to an appropriate theoretical model, an experimental material is also required which allows nanostructural investigations and optical measurements as well.

For the calculations of the optical properties of polymer films with embedded nanoparticles, two routes can be selected. In the exact route, the extinction cross sections $C_{ext}(\tilde{\nu})$ of single particles are calculated. The calculated extinction spectra for single particles—or, better, a summation of various excitation spectra for a particle assembly—can be compared with the experimental spectra of the embedded nanoparticles. In the statistic route, an effective dielectric function $\hat{\varepsilon}(\tilde{\nu})$ is calculated from the dielectric function of the metal $\hat{\varepsilon}_{me}(\tilde{\nu})$ and of the polymer material $\hat{\varepsilon}_{po}(\tilde{\nu})$ by using a mixing formula, the so-called effective medium theory. The optical extinction spectra calculated from the effective dielectric functions by using the Fresnel formulas can be compared with the experimental spectra.

The success of the calculations depends mainly on the introduction of the nanostructural information into the calculation. At both routes of modeling, the nanostructural information can be introduced in different levels. In the first level, only the metal particle filling factor or a mean particle size is introduced. In the next level, also the particle shape is introduced. The best representation of the nanostructure can be reached by introducing the particle size and shape distribution or the size and shape of each single particle into the optical theory.

At both routes, the determination of the size and shape of the nanoparticles is a prerequisite for description of the optical properties. Besides atomic force microscopy (AFM) and scanning electron microscopy (SEM), transmission electron microscopy (TEM) is the most powerful method to determine size and shape distributions of the nanoparticle assemblies. However, extensive sample preparation that is often required can cause preparation effects, and the TEM micrographs sometimes are not representative of the whole nanoparticle-containing insulating material. Therefore, an experimental material is required which can be investigated very easily without extensive TEM preparation.

As such exemplary experimental material, plasma polymer thin films with embedded silver particles are selected [3]. These films were made by simultaneous or alternating plasma polymerization and metal evaporation. The films can be deposited as multilayers consisting of two polymer thin films and a nanoparticle-containing film between these films. Because of the two plasma polymer layers on either side, the particles are completely embedded in a homogeneous media. The multilayer systems are very appropriate for determining particle size and investigating the interface between metal particles and plasma polymer matrix, because here metal nanoparticles are embedded in one plane. This allows a simple determination of the particle size and shape in the TEM.

Moreover, the size and shape of the nanoparticles can be artificially modified by thermally induced processes like reshaping and coalescence without

destroying the polymer matrix. During these processes, the multilayer system remains intact and no material loss takes place. This has the advantage that the optical properties can be described by comparing two nanostructures with the same film thickness and metal content but with different particle size and shape distributions. The introduced two routes for optical computations will be demonstrated by comparing the optical properties of a sample before and after the thermal nanostructural changes.

## 2. EXPERIMENTAL

The multilayer system consisting of plasma polymer thin films with embedded silver particles were deposited by simultaneous plasma polymerization and metal evaporation in a special designed deposition reactor described in reference 3. The nanoparticle-containing plasma polymer films were deposited as multilayer systems with embedded metal particles. The particles are embedded in one plane between two plasma polymer layers without nanoparticles. Since the multilayers have been deposited on glass substrates with a predeposited KCl thin film, the KCl film dissolves in distilled water and the detached film can be caught on common TEM grids. TEM micrographs of these multilayer systems show well-separated single particles. The vertical structure of the multilayers was investigated also by transmission electron microscopy in cross section [4] and XPS depth profiling [5] to confirm the embedding of the silver particles in one plane. Together with TEM micrographs in lateral direction, size and shape of the particles in all three dimensions could be determined.

Size and shape of the embedded particles can be varied during film deposition. They mainly depend on the amount of the evaporated metal, the pressure during the deposition, and the distance of the sample from the metal evaporation source. The particles have a broad size distribution that can be described in principle with a logarithmic-normal distribution [6].

At moderate thermal annealing much below the melting point of the metal particles, substantial changes of the size and shape of the particles were observed [3]: Atomic diffusion processes occur along the grain boundaries and the particle surface (reshaping). If two neighboring particles are closely connected, the particles coalesce and the number of the embedded particles decreases. Additionally, hints of diffusion of metal atoms through the polymer matrix (Ostwald-ripening) were found.

During thermal treatment inside the electron microscope, changes in the particle size and shape can be observed *in situ* [7]. The samples are placed on a sample heating unit and heated up to a certain temperature. However, if the electron beam is fixed during thermal annealing inside the electron microscope at one sample position, matrix changes and contamination were found. In the

following, this sample part is called an irradiated part. This local contamination caused hardening of the polymer matrix. In this case, the thermally induced coalescence and reshaping of the metal particles takes place at higher temperatures compared to the nonirradiated parts of the samples. So, at one sample two nanostructural states can be observed: at the irradiated part the *frozen* deposited nanostructure and outside from the irradiated part the nanostructure after thermal treatment.

Figure 6.1 shows a TEM micrograph of a sample prepared as described above and treated with electron beam irradiation and *in situ* annealing in the electron microscope. Electron microscopy was carried out using a Philips electron microscope CM 20 FEG at 200-kV acceleration voltage. The electron beam was placed on the left part of the sample (left part of Figure 6.1) during annealing. The maximum temperature on the sample holder was 770 K; but due to the low thermal conductivity of the sample, we suppose that the real temperature at the investigated sample region was lower. Because of contamination and hardening of the polymer matrix by electron beam irradiation during the thermal annealing, the nanostructure of the irradiated sample part has remained as deposited, also after thermal annealing. The right part of Figure 6.1 shows the nanostructure of the sample part without electron beam irradiation during thermal annealing. At this sample part, thermally induced reshaping of the silver particles took place. So, Figure 6.1 shows the silver particle sizes and shapes before (*left*) and after (*right*) reshaping.

In order to obtain quantitative results about the size and shape distribution of the embedded particles, both sides of the TEM micrograph were analyzed

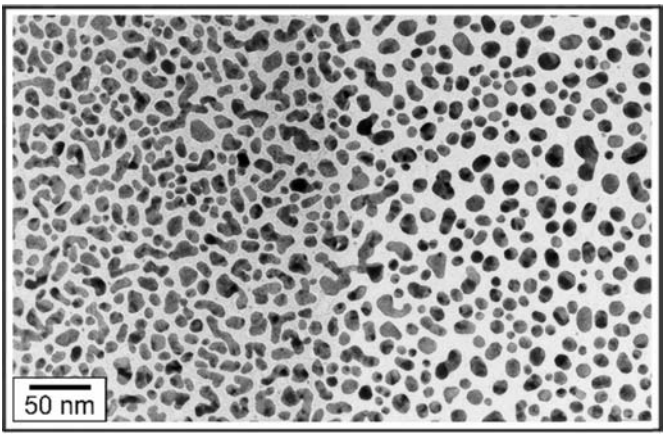


Figure 6.1. TEM micrograph of a plasma polymer multilayer with embedded silver nanoparticles depicting a nanostucture before (**left**) and after (**right**) reshaping and coalescence.

with an optical image processing system. Based on the pixel coordinates of the digital image, area v and perimeter u as well as the center of gravity of each particle were calculated. For approximately spherical particles, the particle size $D$ is given as the mean value of 36 lines of intersections (ferets) $F_n(n)$ as particle projections at different angles $D = \frac{1}{36}\sum_{n=1}^{36} d_n F_n$. For particles with large deviations from the spherical shape, the shape factor $S = 4\pi Ar/U^2$ or the aspect ratio $R = F_{min}/F_{max}$, where $F_{min}$ and $F_{max}$ represent the minimal and maximal feret, have to be calculated additionally for particle form characterization [8]. With respect to the results of the cross-sectional TEM examination, the particles are depicted as elongated spheroids (rotational symmetric ellipsoids), which are described by the mean half-axis A (major axis) and the lower half-axis $B$ (minor axis).

From Figure 6.1, 368 particles were analyzed both before and after annealing, and the results are given in two three-dimensional histograms (Figure 6.2). The $x$ direction gives the minor axis $B$, the $y$ direction gives the major axis $A$, and the $z$ direction gives the number of particles found in the $A$–$B$ interval (count). In particular in the left histogram, there is an important number of large particles with eccentricities $e = B/A < 1$. In the right histogram, the eccentricities of the particles are increased and the particle shapes are closer to the spherical shape ($A \approx B$). This is obviously a result of thermally induced reshaping. The optical computations in the following sections are demonstrated on two different particle assemblies. The two assemblies have different particle size and shape distributions, but the amount of silver in the multilayer system is exactly the same.

In Figure 6.3, the optical extinction spectra before and after thermal annealing are plotted for a comparable film sample that was deposited on quartz

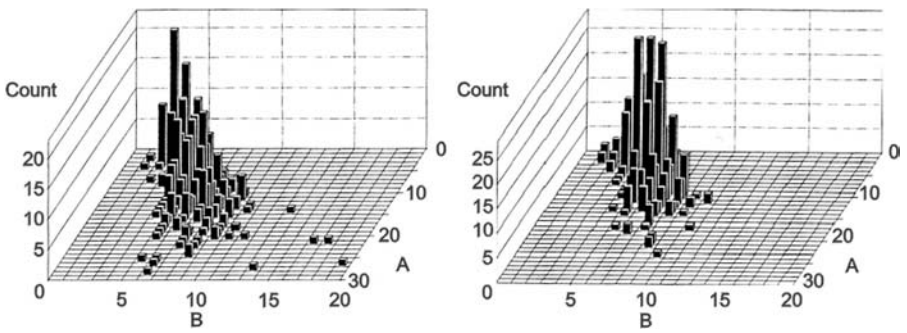


Figure 6.2. Histograms of the mean and lower half-axis for the silver particles from Figure 6.1: for the particles as deposited (**left**) and for the particles after coalescence and reshapening (**right**).

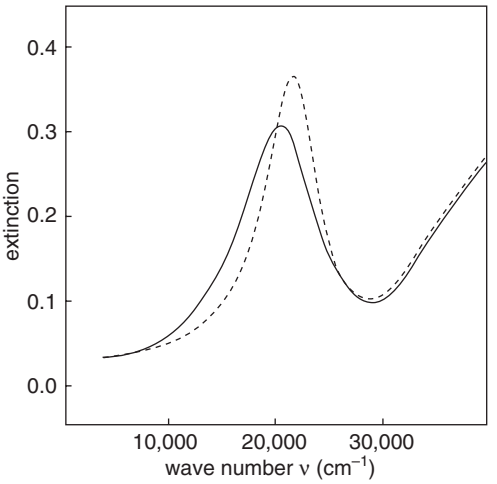


Figure 6.3. Measured extinction spectra before (solid line) and after (dashed line) thermal treatment.

substrates. The spectra were measured with a commonly used spectrophotometer in the spectral region between 4000 $cm^{-1}$ and 50,000 $cm^{-1}$. Thermal treatment was performed under vacuum conditions ($10^{-3}$ Pa) up to 480 K. If the particle size and shape change due to thermal annealing, changes of the plasma resonance absorption are expected. For silver particles embedded in a plasma polymer matrix, a shift of the plasmon position to higher wave numbers (blue shift) and a decrease of the half-width of the plasma resonance absorption were found. The plasma resonance absorption reaches a peak at $\tilde{\nu}_r = 20{,}410\,cm^{-1}$ before annealing and at $\tilde{\nu}_r = 21{,}740\,cm^{-1}$ after annealing. This means that the extinction peak shifts with $\Delta\tilde{\nu}_r = 1330\,cm^{-1}$ to higher wave numbers. In addition, the half-width of the plasma resonance absorption which was determined by Lorentz peak fitting, decreases from $\Gamma = 5450\,cm^{-1}$ to $\Gamma = 4130\,cm^{-1}$. Based on the experimental spectra from Figure 6.3, the results of the optical computations will be discussed in the next two sections.

## 3. OPTICAL COMPUTATIONS IN EXACT ROUTE

For the calculations of the optical properties of polymer films with embedded particles in the exact route, the extinction cross sections $C_{ext}(\tilde{\nu})$ of single particles were calculated based on the solution of the Maxwell equations for spherical particles which is the Mie theory [9, 10]. To reduce the effort for the calculations, often the quasi-static approximation (Rayleigh theory), which con-

siders only dipole excitations, is used. The Rayleigh–Gans theory is a quasi-static approximation for nonspherical particles and includes the Rayleigh theory, which is only valid for spherical particles.

For only a few particle geometries, rigorous solutions for the extinction and scattering of particles are available (spheres: Mie theory [9], spheroids [11], infinite cylinder [12, 13]); the spectra of other particles must be described using approximations. In the Rayleigh approximation, Gans [14] developed a model for ellipsoidal particles, and Fuchs [15] developed a model for cubic particles. Both are based on the calculation of a dipole polarizability of the particle. In the following, the theory of Gans is introduced.

In the Rayleigh approximation, the particle is so small that an applied electric field $\vec{E}_0$ only induces a dipole with dipole moment $\vec{p}$ in the particle. In general, $\vec{E}_0$ and $\vec{p}$ must not be collinear, meaning that the polarizability $\hat{\alpha}$ of the particle is a tensor:

$$\vec{p} = \in_0 \in_m \hat{\alpha} \vec{E}_0 \tag{1}$$

In this notation, the elements of the polarizability tensor are only proportional to the particle volume, similar to the atomic polarizability. $\in_m$ is the dielectric constant of the surrounding medium. A dipole with linear response oscillates with the same frequency as the applied electric field and, hence, emits an electric field $\vec{E}_s$ asymptotically given in the far field as

$$\vec{E}_s = \frac{e^{ikr}}{ikr} \frac{ik^3}{4\pi \in_0 \in_m} \vec{e}_r \times (\vec{e}_r \times \vec{p}) \tag{2}$$

Using Poynting's theorem, finally, after some mathematics, the extinction cross section $C_{\text{ext}}$ for the dipole is obtained as

$$C_{\text{ext}} = k \,\text{Im} \sum_{i=1}^{3} \sum_{j=1}^{3} \alpha_{ij} e_i e_j \tag{3}$$

Im means the imaginary part, and $e_i$ and $e_j$ are the normalized components of the incident field vector. For an ellipsoidal particle with three different elementary axes $A$, $B$, and $C$, the polarizability tensor only has diagonal elements $\alpha_{jj}$, with

$$\alpha_{jj} = 4\pi ABC \frac{\in(\omega) - \in_m(\omega)}{\in_m(\omega) + G_j(\in(\omega) - \in_m(\omega))} \tag{4}$$

$G_j$ are factors taking into account the geometry of the ellipsoid. They satisfy the conditions

$$\sum G_j = 1, \qquad G_j \le 1 \quad \forall j \tag{5}$$

For comparison with the experiments, the special case of spheroids has been found suitable. They are characterized by coincidence of two of the three elementary axes. One distinguishes elongated or prolate spheroids with $B = C$ and distinguishes flattened or oblate spheroids with $A = B$. In the following, $A$ is always the major axis and $B$ the minor axis of the spheroid. Accordingly, only two factors $G_1(e)$ and $G_2(e)$ are relevant, depending on the eccentricity $e$, defined for a spheroid as

$$e^2 = 1 - \left(\frac{B}{A}\right)^2 \tag{6}$$

$G_1$ differs for prolate and oblate spheroids:

$$\textit{prolate}: \qquad G_1(e) = -g(e)^2\left\{1 - \frac{1}{2e}\ln\left(\frac{1+e}{1-e}\right)\right\} \tag{7}$$

$$\textit{oblate}: \qquad G_1(e) = \frac{g(e)}{2e^2}\left\{\frac{\pi}{2} - \tan(g(e))^{-1}\right\} - \frac{g(e)^2}{2} \tag{8}$$

with

$$g^2(e) = \frac{1-e^2}{e^2} \tag{9}$$

In Figure 6.4, $G_1(e)$ is plotted versus the eccentricity e for prolate and oblate spheroids. It starts with $G_1(0) = \frac{1}{3}$, which is the case of a spherical particle ($A$

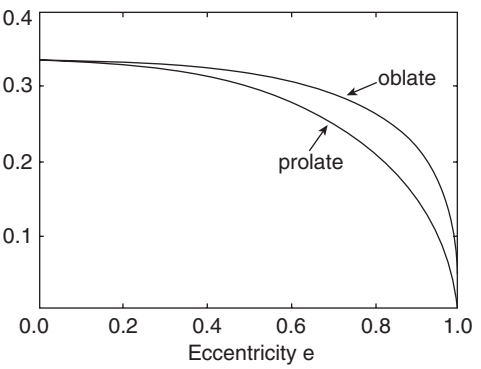


Figure 6.4. Geometry factor $G_1(e)$ as a function of the eccentricity $e$.

$= B = C$) and decreases with increasing eccentricity. Vice versa, following from equation (5), $G_2(e)$ also starts with $G_2(0) = \frac{1}{3}$, but it increases with increasing eccentricity. It follows now from equation (4) that for a spheroidal silver particle, two surface plasma resonances are induced, namely, when the optical constants of silver satisfy the conditions

$$\epsilon(\omega) = -\epsilon_m \frac{1 - G_j}{G_j} \tag{10}$$

For simplicity, consider the dielectric constant to be purely a Drude dielectric constant without damping, that is,

$$\epsilon(\omega) = 1 - \frac{\omega_p^2}{\omega^2} \tag{11}$$

where $\omega_p$ is the plasma frequency of the free electrons. Then, it becomes obvious that the plasma resonance for $G_1$ contributes to the spectrum at lower frequencies, while the plasma resonance for $G_2$ contributes at higher frequencies than the frequency at which the plasma resonance of the equivalent volume sphere with $G_1 = G_2 = \frac{1}{3}$ is peaked.

The optical extinction spectra for prolate spheroids were computed using optical constants of silver from references 16 and 17, taking into account additional damping of the plasma resonance absorption according to the model of the mean free path effect. Figure 6.5 gives a section enlargement of Figure 6.1, left, from the particles as deposited. Five particles are marked. The major axis $A$, the minor axis $B$, and eccentricities $e$ are given as follows:

| | | | |
|---|---|---|---|
| Particle 1: | $A = 9.7\,\text{nm}$, | $B = 7.3\,\text{nm}$, | $e = 0.66$ |
| Particle 2: | $A = 12.1\,\text{nm}$, | $B = 11.0\,\text{nm}$, | $e = 0.41$ |
| Particle 3: | $A = 21.0\,\text{nm}$, | $B = 7.0\,\text{nm}$, | $e = 0.94$ |
| Particle 4: | $A = 23.6\,\text{nm}$, | $B = 13.1\,\text{nm}$, | $e = 0.83$ |
| Particle 5: | $A = 33.9\,\text{nm}$, | $B = 6.8\,\text{nm}$, | $e = 0.98$ |

Figure 6.6 shows the calculated extinction spectra of these five selected particles. Peak position and magnitude of the $G_1$ mode obviously depend on the shape and size of the corresponding particle. The larger the eccentricity of the particle, the lower the wave number where the plasma resonance absorption of the $G_1$ mode is peaked. The peak magnitude approximately correlates with the particle volume, but for a quantitative comparison the dispersion of the optical constants in the polarizability must be taken into account. For that reason, the absorption peak magnitude of the larger particle 5 is smaller than the magnitude of particle 4, although its volume is larger than that of particle 4.

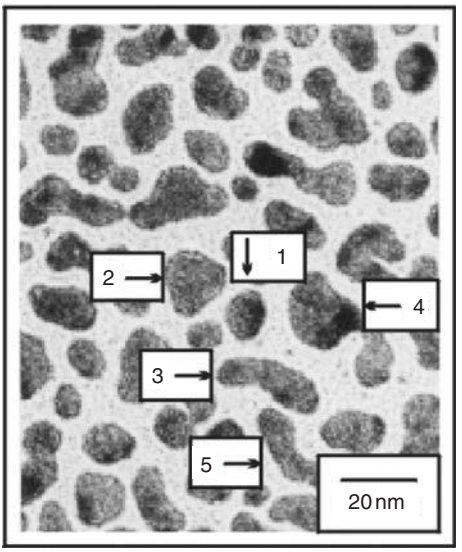


Figure 6.5. TEM micrograph of embedded silver nanoparticles (section enlargements from Figure 6.1).

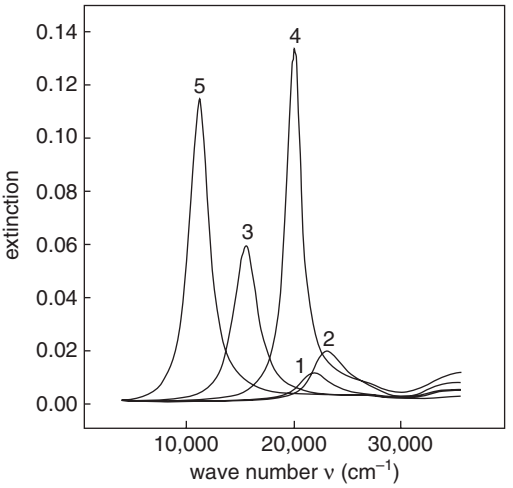


Figure 6.6. Extinction spectra of five single particles, as marked in Figure 6.5.

In Figure 6.7, computed extinction spectra for the particle assemblies before and after the nanostructural changes are presented. The results from image analysis are used to compute extinction spectra of 368 particles with varying size parameters; the total spectra of the sample are added up before (solid curve)

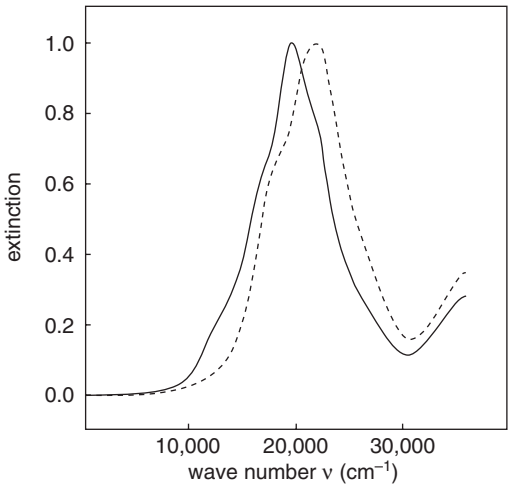


Figure 6.7. Calculated extinction spectra added up for 368 particles before (solid curve) and 368 particles after (dashed curve) thermal treatment, respectively.

and after thermal (dashed curve) treatment. For better comparison the spectra are normalized.

It is obvious that the calculated spectrum of the sample after thermal treatment is blue-shifted with a shift of $\Delta\tilde{\nu}_r = 1570\,\mathrm{cm}^{-1}$. The peak positions before and after thermal treatment are $\tilde{\nu}_r = 19{,}420\,\mathrm{cm}^{-1}$ and $\tilde{\nu}_r = 21{,}050\,\mathrm{cm}^{-1}$, in good agreement with our experimental data at Figure 6.3. At the experimental spectra, the plasma resonance absorption is peaked at $\tilde{\nu}_r = 20{,}410\,\mathrm{cm}^{-1}$ before and at $\tilde{\nu}_r = 21{,}740\,\mathrm{cm}^{-1}$ after thermal treatment. This means that the experimental extinction peak shifts with $\Delta\tilde{\nu}_r = 1330\,\mathrm{cm}^{-1}$ to higher wave numbers. The half-widths with $\Delta\tilde{\nu}_r = 7200\,\mathrm{cm}^{-1}$ and $\Delta\tilde{\nu}_r = 6730\,\mathrm{cm}^{-1}$ are larger than the measured half-widths of $\Gamma = 5450\,\mathrm{cm}^{-1}$ and $\Gamma = 4130\,\mathrm{cm}^{-1}$, respectively. One possible reason for this divergence is that the particles that have a more complicated shape are projected to ellipsoids. Another reason may be that the computed spectra exhibit resonances at lower wave numbers which are missing in the measured spectra in Figure 6.3. They are caused by the restricted validity of the used model in the computations. For silver particles with sizes exceeding about 20 nm, the Rayleigh approximation is not more valid and more precise computations are needed.

The agreement between the experimental and calculated spectra is rather good. The calculations give a good explanation of the blue shift of the plasma resonance absorption of the silver nanoparticles due to their nanostructural changes during the thermal treatment. In the computations with the

Rayleigh–Gans theory, the values for major and minor particle half-axes were used for each single particle. The nanostructural information given from the TEM micrographs was very well considered for the optical calculations.

## 4. OPTICAL COMPUTATIONS IN THE STATISTICAL ROUTE

In the statistic route, an effective dielectric function $\hat{\varepsilon}(\tilde{\nu})$ is calculated from the dielectric function of the metal $\hat{\varepsilon}_{me}(\tilde{\nu})$ and the of polymer material $\hat{\varepsilon}_{po}(\tilde{\nu})$ by using a formula, the effective medium theory. The most general effective medium theory is the Bergman theory in which the nanostructure of the composite material can be considered by a spectral density function. The Bergman theory includes the solutions from the Bruggeman theory and the Maxwell Garnett theory for spherical, parallel-oriented, and random-oriented ellipsoidal particles.

In addition to the volume filling factor, some theories include parameters that describe nanostructure—for example, the depolarization factor $L$ or the spectral density $g(x)$. If the nanostructure is unknown, these parameters and the filling factor act only as fit parameters. If the calculations fit well to the experimental data, it is possible to obtain information about an unknown nanostructures, although there are situations where this can be misleading.

The most popular effective medium theories are the Maxwell Garnett theory [18], which was derived from the classical scattering theory, and the Bruggeman theory [19]. With these theories, an effective dielectric function is calculated from the dielectric functions of both basic materials by using the volume filling factor. At some extensions of these theories, a unique particle shape for all particles is assumed. There is also an other concept based on borders for the effective dielectric functions. The borders are valid for a special nanostructure. Between these borders, the effective dielectric function varies depending on the nanostructure of the material. The Bergman theory includes a spectral density function $g(x)$ that is used as fit function and correlates with the nanostructure of the material [20].

In 1906, J. C. Maxwell Garnett used the Maxwell Garnett theory, equation (12), for the first time to descibe the color of metal colloids glasses and of thin metal films. Equation (12) can be deviated from the Rayleigh scattering theory for spherical particles [21], or from the Lorentz–Lorenz assumption for the electrical field of a sphere and the Clausius–Mossotti Equation by using the polarizability of an metal particle if only dipole polarization is considered [22].

The Maxwell Garnett theory is expressed as

$$\frac{\hat{\varepsilon}(\tilde{\nu})-\hat{\varepsilon}_{\mathrm{po}}(\tilde{\nu})}{\hat{\varepsilon}(\tilde{\nu})+2\hat{\varepsilon}_{\mathrm{po}}(\tilde{\nu})}=f\frac{\hat{\varepsilon}_{\mathrm{me}}(\tilde{\nu})-\hat{\varepsilon}_{\mathrm{po}}(\tilde{\nu})}{\hat{\varepsilon}_{\mathrm{me}}(\tilde{\nu})+2\hat{\varepsilon}_{\mathrm{po}}(\tilde{\nu})} \tag{12}$$

where $\hat{\varepsilon}_{\mathrm{me}}(\tilde{\nu})$ is the dielectric function of the metal, $\hat{\varepsilon}_{\mathrm{po}}(\tilde{\nu})$ is the dielectric function of the polymer, $\hat{\varepsilon}(\tilde{\nu})$ is the effective dielectric function, and $f$ is the volume filling factor; this theory was developed for spherical particles only and without interactions of neighbored particles. All particles are completely encapsulated in an insulation matrix material. A further prerequisite was also that the size of the particles is small in comparison with the wavelength of the incident light. At higher filling factors, the particle–particle interactions can no longer be neglected.

For the case where the particles do not have a spherical shape, various extensions of the Maxwell Garnett theory for nonspherical particles were introduced. The particles are spheroidal with the same shape (ratio of major-axis $A$ and minor axis $B$), but with different sizes still in the wavelength limit. It remains only to choose between a parallel or a random orientation of the mean axis of the ellipsoids.

$$\frac{\hat{\varepsilon}(\tilde{\nu})-\hat{\varepsilon}_{\mathrm{po}}(\tilde{\nu})}{\hat{\varepsilon}_{\mathrm{po}}(\tilde{\nu})+L[\hat{\varepsilon}(\tilde{\nu})-\hat{\varepsilon}_{\mathrm{po}}(\tilde{\nu})]}=f\frac{\hat{\varepsilon}_{\mathrm{me}}(\tilde{\nu})-\hat{\varepsilon}_{\mathrm{po}}(\tilde{\nu})}{\hat{\varepsilon}_{\mathrm{po}}(\tilde{\nu})+L[\hat{\varepsilon}_{\mathrm{me}}(\tilde{\nu})-\hat{\varepsilon}_{\mathrm{po}}(\tilde{\nu})]} \tag{13}$$

At the extensions of the Maxwell Garnett theory for parallel-oriented ellipsoids, equation (13) [23, 24], all particles are ellipsoids with parallel the mean axis. Only one depolarization factor $L$ is necessary. $L$ describes the ratio between the axes of the ellipsoids, and values for $L$ between $0 \le L \le \frac{1}{3}$ (rod), $L = \frac{1}{3}$ (sphere) and $\frac{1}{3} \le L \le 1$ (disk) are possible. For the encapsulation of spherical particles ($L = \frac{1}{3}$), equation (13) gives the same result as the Maxwell Garnett theory, equation (12). For particles embedded in one plane, the orientation of the ellipsoids in ratio to the substrate is parallel or perpendicular to the plane of the incident light. An orientation of the ellipsoidal particles diagonally to the substrate cannot be considered.

$$(1-f)\frac{\hat{\varepsilon}(\tilde{\nu})-\hat{\varepsilon}_{\mathrm{po}}(\tilde{\nu})}{\hat{\varepsilon}_{\mathrm{me}}(\tilde{\nu})-\hat{\varepsilon}(\tilde{\nu})}=\frac{f}{3}\sum_{i=1}^{3}\frac{\hat{\varepsilon}_{\mathrm{po}}(\tilde{\nu})}{\hat{\varepsilon}_{\mathrm{po}}(\tilde{\nu})+[L_i(\hat{\varepsilon}_{\mathrm{me}}(\tilde{\nu})-\hat{\varepsilon}_{\mathrm{po}}(\tilde{\nu})]} \tag{14}$$

The extensions of the Maxwell Garnett theory for random-oriented ellipsoids, equation (14) [25], needs three depolarization factors $L_1$, $L_2$, $L_3$ with $\Sigma L_i = 1$ to describe the embedded ellipsoids. Frequently, ellipsoids with a symmetrical axis of rotation are assumed with $L_2 = L_3$. Extreme geometries are rods with $L_1 \gg L_2 = L_3$ and disks with $L_1 \ll L_2 = L_3$. For $L_i = \frac{1}{3}$, the extensions of the Maxwell Garnett theory for random-oriented ellipsoids, equation (14), give the same result as the Maxwell Garnett theory, equation (12).

There is also another extension of the Maxwell Garnett theory for random-oriented ellipsoids [29] which is different from equation (14). Other extensions of the Maxwell Garnett theory are described for chiral aggregates of spheres [26], for thin films with columnar structures [27], and for embedded spherical particles of several metals [28].

For the following calculation, experimentally determined dielectric functions for silver [30] and for a plasma polymer [31] were taken. The effective dielectric functions $\hat{\varepsilon}(\tilde{\nu})$ were calculated with the Maxwell Garnett theory for parallel-oriented particles, equation (13). From the effective dielectric function, transmission or extinction spectra can be calculated by using the Fresnel formulas [10] for the optical system air–composite media–quartz substrate. As a further parameter, the thickness of the film with embedded particles and the thickness of other present layers that do not contain metal nanoparticles have to be included. The calculated extinction spectra can be compared with the experimental spectra.

For the calculation of the transmission or extinction spectra, the thickness of each layer $d_{p1}$, $d_c$, and $d_{p2}$ must be considered in the right way. In the following, the results from the particle size and shape analysis from the TEM micrograph of Figure 6.1 were transfered to the parameters that are necessary for the effective medium theories. These are the volume filling factor $f$, the depolarization factor $L$, and the composite film thickness $d_c$.

From the image analysis of the lateral TEM micrographs, the area filling factor $F_{fl}$ and the mean values for the particles size $\overline{D}$ and the particle shape $\overline{S}$ are given. The maximum mean particle diameter $\overline{D}_{max}$ is defined with $\overline{D}_{max} = \overline{D} + \sigma_D$. The area filling factor $F_{fl}$ only agrees with the volume filling factor $f$ if the particles have prism shape with ellipsoidal basic area. In the case $f = F_{fl}$, the height of all prisms is equal to the composite film thickness $d_c$.

The cross-sectional TEM investigations have depicted the fact that vertical projection of the particles are also ellipsoids with the diameters $D_A$, $D_B$, and $D_C$. It is useful to assume that two lower diameters are identical ($D_B = D_C$, rotational symmetry). The diameters $\overline{D}_A$ and $\overline{D}_B$ can be calculated from $\overline{D}$ and $\overline{S}$ using $\overline{D}_A = \overline{D}(1+\sqrt{1-\overline{S}})$ and $\overline{D}_B = \overline{D}(1-\sqrt{1-\overline{S}})$.

By comparison of the ratio of prism volume to the ellipsoid volume, a maximal volume filling factor $f_{max}$ follows from the area filling factor using $f_{max} = \frac{2}{3}F_{fl}$. This upper bound of the volume filling factor is valid if all particles have an identical size of $\overline{D}_{max}$. In this case, the minimum composite film thickness corresponds with the mean vertical diameter of the particles $d_{c_{min}} = \overline{D}_B$ if all particles lie exactly in one plane. Because there is a statistical particle size distribution, the composite film thickness must be defined from the maximal vertical diameter of the largest particle $d_{c_{max}} = D_{B_{max}} \cdot D_{B_{max}}$ can be obtained from the image analysis data. It is better to calculate $D_{B_{max}}$ with $D_{B_{max}} = D_{max}(1-\sqrt{1-S_{max}})$. The filling factor $f$ is decreased further by the ratio between the mean particle

diameter $\overline{D}_B$ and maximum vertical particle diameter $D_{B_{\max}}$ with $f_{\min} = (\overline{D}_B/D_{B_{\max}})^{\frac{2}{3}} F_{\mathrm{fl}}$. Based on this geometrical assumptions, the lower and the upper bound $f_{\min} \le f \le f_{\max}$ act a criteria for the success of the calculations with the effective medium theories.

The depolarization factor $L$ in equation (13) as well as the depolarization factors $L_i$ in equation (14) can be calculated from the mean aspect ratio $\overline{Q}$ of the particles as well as from the mean shape factor $\overline{S}$. For ellipsoids with three doubled half-axes $\overline{D}_A$, $\overline{D}_B$, and $\overline{D}_C$, $L_i$ is given by equation (15) [23].

$$L_i = \frac{\overline{D}_A, \overline{D}_B, \overline{D}_C}{16} \int \frac{du}{(\overline{D}_i + 4u)\sqrt{(\overline{D}_A^2 + 4u)(\overline{D}_B^2 + 4u)(\overline{D}_C^2 + 4u)}} \tag{15}$$

With equation (15) the depolarization factors $L$ and $L_i$ can be calculated from the mean shape factor $\overline{S}$. In the left part of Figure 6.8, $L$ as a function from $S$ is given. The lower curve is valid for rods ($L < \frac{1}{3}$), and the upper curve is valid for disks ($L > \frac{1}{3}$). The depolarization factors $L_i$ for rods ($L_1 > L_2 = L_3$) and for plates ($L_1 < L_2 = L_3$) are also given in Figure 6.8. For rods, the depolarization factor $L_1$ is given from the upper curve in the left part of Figure 6.8, while $L_2 = L_3$ is given from the lower curve. For disks, the right part of Figure 6.8 is valid. $L_1$ is given from the lower curve, and $L_2 = L_3$ is given from the upper curve.

Figure 6.9 presents two calculated optical extinction spectra. The spectra can be compared to the spectra from Figure 6.3. Based on the results from the image analysis and the considerations concerning the filling factor and the depolarization factors, the following parameters were used. Spectra before reshaping: $d_{\mathrm{p1}} = 40\,\mathrm{nm}$, $d_{\mathrm{c}} = 10\,\mathrm{nm}$, $d_{\mathrm{p2}} = 40\,\mathrm{nm}$, $f = 0.2$, and $L = 0.21$. Spectra after reshaping: $d_{\mathrm{p1}} = 38\,\mathrm{nm}$, $d_{\mathrm{c}} = 13\,\mathrm{nm}$, $d_{\mathrm{p2}} = 39\,\mathrm{nm}$, $f = 0.15$, and $L = 0.25$. The decrease of the area filling factor in the coalesced part in Figure 6.1 was compensated by an increase of the composite film thickness. The spectral positions

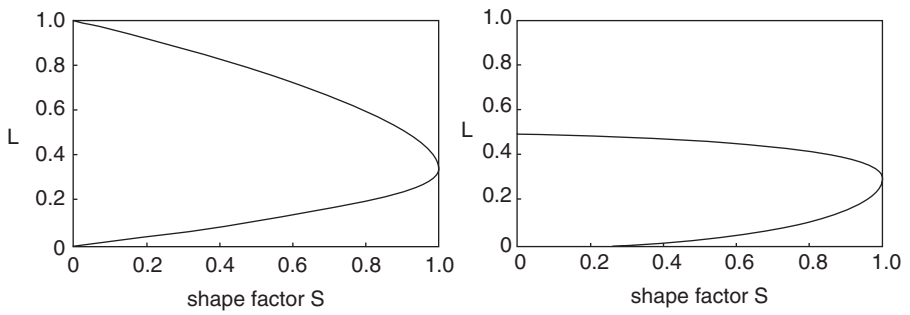


Figure 6.8. $L$ and $L_i$ as a function of the particle shape factor $S$.

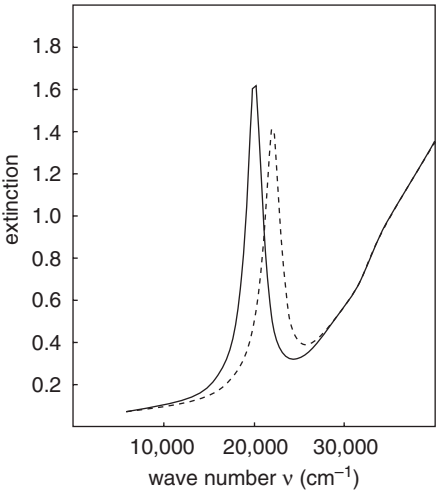


Figure 6.9. Calculated extinction spectra (Maxwell Garnett theory) for parallel-oriented ellipsoids before (solid curve) and after (dashed curve) thermal treatment.

at $\tilde{\nu}_r = 20{,}200\,\mathrm{cm}^{-1}$ before and at $\tilde{\nu}_r = 21{,}900\,\mathrm{cm}^{-1}$ of the plasmon resonance are comparable to the spectral positions in the experimental spectra, the plasma extinction peak shifts with $\Delta\tilde{\nu}_r = 1700\,\mathrm{cm}^{-1}$ to higher wave numbers. This is in good agreement with the experimental spectra of Figure 6.3, but obviously the half-width is too low. The blue shift that occurs at reshaping was reproduced successfully under consideration of different depolarization factors. However, in the effective medium theory the depolarizcation factor that represents the nanostructure can only be used as mean value for all particles.

## 5. SUMMARY

In this chapter, two different routes for modeling of the optical properties of nanoparticles embedded in thin polymer films were presented. Both routes can give comparable results. The only difference between the Rayleigh theory and the Maxwell Garnett theory for spherical particles, respectively, is the different mathematical formulation. The calculated spectra are comparable. In principle, this must be noted also for the Rayleigh Gans theory and the Maxwell Garnett theory for parallel-oriented ellipsoidal particles. The difference is only in which way the nanostructural information is introduced. This is done in the Rayleigh Gans theory as the size and shape of each single particle and in the Maxwell Garnett theory as statistical particle size and shape distribution for the particle assembly. However, in the effective medium theory the depolar-

ization factor can only be used as mean value for all particles. Therefore, the computation of optical spectra of single particles that are characterized by image processing and the summation of all contributions to a complete spectrum can be preferred.

The presented computations demonstrated passable ways to describe the optical properties of embedded nanoparticles. If reliable nanostructural information is given, computation can be successful without extensive effort. Commercial programs for the presented calculations are available. For a more precise description of nanoparticle-containing insulating materials, the implementation of the nanostructural information given by electron microscopy has to be introduced in a more detailed manner into the optical theory, the computational effort must increase enormously, and it cannot be ensured that qualitatively new results will be reached. Furthermore, in most cases, computational results for one experimental system cannot be copied easily to an other experimental system. The presented computations show a recommended shortcut for optical modeling that can be used for a large number of nanoparticle-containing insulating materials. Depending on the kind of material and the given nanostructural information, the computations will result in a more or less good attempt to determine the relationship between nanostructure and optical plasmon resonance for embedded nanoparticles.

## REFERENCES


1. H. Raether, *Surface Plasmons*, Springer Tracts in Modern Physics Vol. 111, Springer, Berlin (1988).
2. U. Kreibig, and M. Vollmer, *Optical Properties of Metal Clusters*, Springer Series in Material Science, Vol. 25, Springer, Berlin (1995).
3. A. Heilmann, *Polymer Films with Embedded Metal Nanoparticles*, Springers Series in Materials Science, Vol. 52, Springer, Heidelberg (2002).
4. W. Grünewald, A. Heilmann, and C. Reinhardt, *Appl. Surf. Sci.* **93**, 157 (1996).
5 A. Heilmann, J. Werner, M. Kelly, B. Holloway, and E. Kay, *Appl. Surf. Sci.* **115**, 365 (1997).
6. C. G. Granqvist and R. A. Buhrman, *J. Appl. Phys.* **47**, 2200 (1976).
7. A. Heilmann and J. Werner, *Thin Solid Films* **317**, 21 (1998).
8. A. Heilmann, J. Werner, D. Schwarzenberg, S. Henkel, P. Grosse and W. Theiss, *Thin Solid Films*, **270**, 103 (1995).
9. G. Mie, *Ann. Phys.* **25**, 377 (1908).
10. C. F. Bohren, and D. R. Huffman, *Absorption and Scattering by Small Particles*, Wiley, New York (1983).
11. S. Asano, and G. Yamamoto, *Appl. Opt.* **14**, 29 (1975).
12. W. Seitz, *Ann. Phys.* **21**, 1013 (1906).

13. W. von Ignatowski, *Ann. Phys.* **18**, 495 (1905).
14. R. Gans, *Ann. Phys.* **37**, 881 (1912).
15. R. Fuchs, *Phys. Rev. B* **11**, 1732 (1975).
16. M. Quinten and U. Kreibig, *Appl. Opt.* **32**, 6173 (1993).
17. M. Quinten, *Z. Phys. B* **101**, 211 (1996).
18. J. C. M. Garnett, *Philos. Trans. Royal Society London* **203**, 385 (1904); **205**, 237 (1906).
19. D. A. G. Bruggeman, *Ann. Phys.* **24**, 636 (1935).
20. D. J. Bergman, *Phys. Rev. B* **23**, 3058 (1981); *Phys. Rep. (Phys. Lett. C)* **43**, 377 (1978).
21. Lord J. W. Rayleigh, *Philos. Mag.* **34**, 481 (1892).
22. C. Kittel, *Introduction to Solid State Physics*, Wiley, New York (1995).
23. D. Polder and J. H. van Santen, *Physica* **XII**, 257 (1946).
24. R. W. Cohen, G. D. Cody, M. D. Coutts, and B. Abeles, *Phys. Rev. B* **8**, 3689 (1973).
25. H. Fricke, *Phys. Rev.* **24**, 575 (1924).
26. A. H. Shivola and I. V. Lindell, *Electr. Lett.* **26**, 119 (1990).
27. G. B. Smith, *Opt. Commun.* **71**, 279 (1989).
28. D. E. Aspnes, *Thin Solid Films* **89**, 249 (1982).
29. C. G. Granqvist and O. Hunderi, *Phys. Rev. B* **18**, 2897 (1978).
30. P. B. Johnson and R. W. Christy: *Phys. Rev. B* **6**, 4370 (1972).
31. A. Heilmann, G. Kampfrath, and V. Hopfe, *J. Phys. D* **21**, 986 (1988).